ON THE DIMINISHING RETURNS OF THERMAL CAMERA RESOLUTION FOR PBF TEMPERATURE ESTIMATION

Nathaniel Wood¹, Edwin Schwalbach*², Andrew Gillman^{†2}, and David J. Hoelzle ^{‡1}

¹Department of Mechanical and Aerospace Engineering, the Ohio State University, Columbus, OH 43210

²Air Force Research Laboratory, Dayton, OH, 45433-5519 USA

Abstract

Powder Bed Fusion (PBF) faces ongoing challenges in the areas of process monitoring and control. Standard methods for alleviating these issues rely on machine learning, which requires costly and time-consuming training data. Expense is compounded by the perceived necessity of using sensors with extremely high resolutions. This research avoids this cost by employing an Ensemble Kalman Filter (EnKF), which uses measured data to correct physics-based model predictions of the process, to monitor part internal temperature fields during building. This work tests EnKF performance, in simulation, for two model architectures, using simulated cameras of varying resolution as our measuring instruments. Crucially, we show that increasing camera resolution produces diminishing returns in EnKF accuracy, relative to the model predictions, with up to 81% error reduction. This result shows that current AM quality control practices with expensive sensors may be inefficient; with appropriate algorithms, cheaper setups may be used with little additional error.

1 Introduction

Powder Bed Fusion (PBF) is a type of additive manufacturing (AM) process that builds parts out of successive layers of metal powder in a layer-by-layer fashion. The process, Fig. 1, has three stages. First, a layer of powder is swept over the machine base plate or a previous layer of powder. Second, the machine heat source, either an electron beam (E-PBF, Fig. 1a) or a laser beam (L-PBF, Fig. 1), traces a 2D pattern on top of the powder. The heat source welds the powder, creating a region of fused material within the powder layer. Third, the base plate is indexed in the -z direction, allowing a new layer of powder to be swept atop the old, and beginning the cycle anew.

^{*}email: edwin.schwalbach@us.af.mil

[†]email: andrew.gillman.2@us.af.mil

[‡]Corresponding author. Phone: +1 (614) 688-2942; email: hoelzle.1@osu.edu

AM has demonstrated rapid adoption by industry [3], and is projected to induce broad changes to supply chains and product design in the near future [4] as it rapidly expands its' market size [5]. PBF shares the features of AM that drive this impact. These include producing parts with unparalleled geometric complexity, moving increasing amounts of production on-site, and removing barriers to frequent changes in product design ("customization for free") [3]. Despite these advantages, applying PBF to applications that demand strict quality control (QC) remains a challenge, due to PBF-produced parts commonly exhibiting defects. These flaws include anisotropic material properties ([6, 7]), arising from irregular microstructures ([8-10]), large residual stresses ([11–13]), and porosity ([14–18]). Historically, PBF QC has struggled with detecting and mitigating these defects.

Industry-standard PBF QC techniques involve identifying an appropriate range for the relevant process parameters, and then checking the part for defects after building is complete. Historically, parameter ranges have been identified with extensive design of experiments (DOE) studies [19–21]. Prototype QC approaches use machine learning to help identify these ranges [22, 23], as well as to detect certain process defects in-situ [24, 25]. Both these approaches are time-consuming and expensive, either because of running the DOE studies or

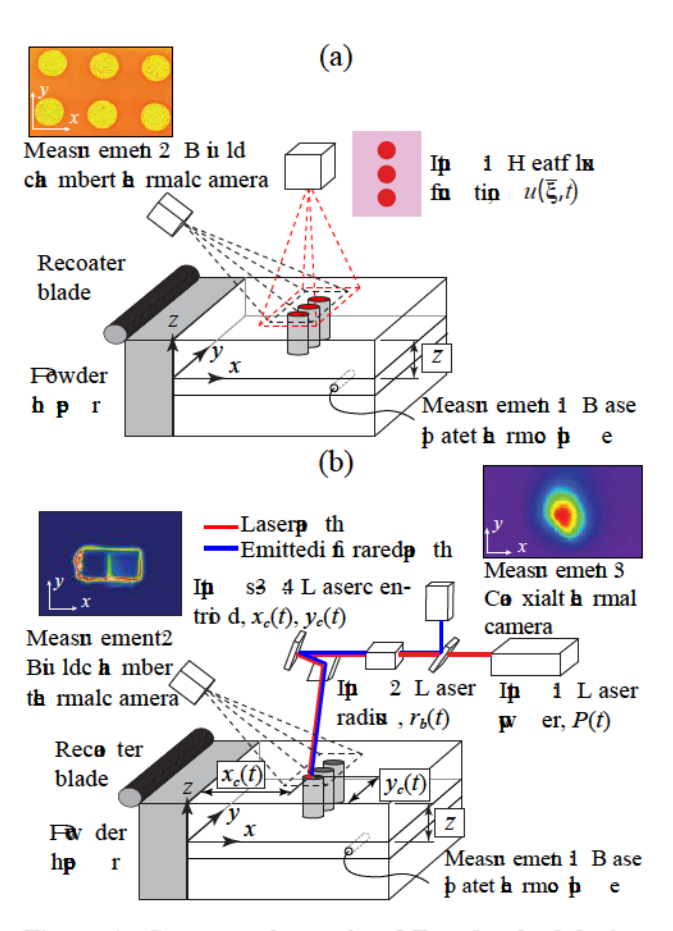


Figure 1: System schematic of Powder bed fusion (PBF) additive manufacturing. Reproduced from [1] with permission from IEEE. (a) Input and output channels for E-PBF. Measurement 2 screenshot reproduced from [2] with permission from The Minerals, Metals, and Materials Society. (b) Input and output channels for L-PBF and E-PBF with a slow raster speed.

training the data-driven algorithms. Furthermore, they are inflexible. The parameter ranges and/or algorithms must be reset for any nontrivial change in processing environment, such as changing the part geometry, part material, or even the machine being used. This inflexibility could be mitigated by factoring physics-based models into the algorithms being trained, wherein changes in the processing environment are modeled easily in software [24,26,27]. Although computationally efficient strategies are being developed [28,29], historically these physics-based models have been far too computationally expensive to run in-situ [23,30]. A new paradigm is needed, which combines the accuracy of data-driven algorithms with the flexibility of physics-based models, without needing exhaustive datasets and without sacrificing computational efficiency.

This paper examines state estimation as a candidate for this new paradigm. State estimators are a class of control theory algorithms that take physics-based models of the process, and correct

the model estimations with in-situ process measurements. The estimator algorithm we implement in this work is an Ensemble Kalman Filter (EnKF) [31], which supplies approximately 2-norm optimal estimations of the process without needing a priori knowledge like machine learning algorithms. The process we model is a 3D representation of PBF thermal physics, for certain E-PBF and L-PBF configurations. These are simplified, linear models, to maximize computational efficiency of the algorithm. Our "in-situ" measurements are a set of simulated thermal cameras that have a varying amount of pixels, which we denote as p. The camera architectures differ for the E-PBF and L-PBf configurations, and "image" the temperature fields of a more accurate, nonlinear model of the same thermal physics. We simulate inaccurate knowledge of the process environment by constructing the nonlinear model with different material properties than the linear models. We test the ability of the EnKF to remove the errors caused by inaccurately-known material properties, and model linearization, as a function of the model configuration and of p. By testing in simulation, we limit the number of uncontrolled variables, and enable the use of error metrics that would be impossible to implement with a physical test. In doing so, we build on the work of [1,32], where we derive our process models and some of their control theory properties, and test the performance of the EnKF on 2D instances of these models, respectively.

The rest of this paper is organized as follows. In Section 2, we derive our physics-based models and present our EnKF algorithm, Algorithm 1. In Section 3, we detail the setup parameters and procedures of our tests. Section 4 analyzes the results of these tests. We conclude our discussion with Section 5, and supply directions of future work in this area.

2 Algorithm details

In this section we detail the operation of our EnKF algorithm. Section 2.1 lists the assumptions that underlie our PBF thermal model. In Section 2.2, we construct the (nonlinear) thermal model, and produce two linear models from it. Sections 2.1-2.2 summarize our work in [32]; interested readers should consult this publication for more detail. In Section 2.3, we apply the EnKF to these models to correct for inaccuracies in the linear model estimations.

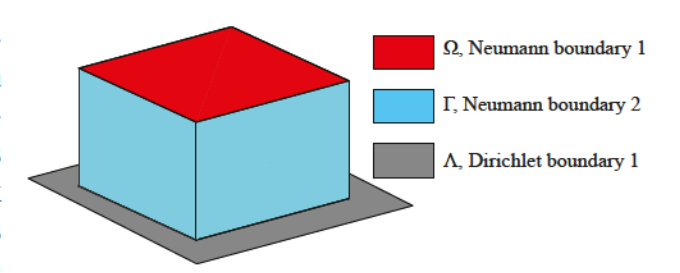


Figure 2: Description of PBF boundary conditions for a simple part.

2.1 Model assumptions

We describe the part geometry as a volume $V \subset \mathbb{R}^3$, with the 3D spatial coordinate represented by $\xi = [x, y, z]'$. As demonstrated in Fig. 2, we divide the boundary of V into three parts, $S = \{\Lambda, \Gamma, \Omega\}$. Surfaces $\Lambda = \{\underline{\xi} : z = 0\}$ are the bottom faces of V. Surfaces $\Omega = \{\bar{\xi} : z = z_{\text{max}}\}$ are the top faces of V. Surfaces Γ represent all other bounding faces of V. Within V, we model PBF

heat transfer according to the flux balance (1). Here, $T(\xi,t)$ is the temperature at $\xi \in V$, at time $t \ge 0$. In (1), the flux from the heat source, $u(\bar{\xi},t)$, (2), only takes nonzero values for $\xi \in \Omega$, which we denote as $\bar{\xi}$. In (2), P(t) is the source power, $r_b(t)$ is the source beam radius, and $x_c(t)$ and $y_c(t)$ are the coordinates of the heat source centerpoint.

$$\rho c \frac{\partial T(\xi, t)}{\partial t} = u(\bar{\xi}, t) - q_{\text{cond}} - q_{\text{conv}} - q_{\text{rad}}, \tag{1}$$

$$u(\bar{\xi},t) = \frac{P(t)}{r_b^2(t)} \exp\left(-\frac{(x_{\bar{\xi}} - x_c(t))^2 + (y_{\bar{\xi}} - y_c(t))^2}{2r_b^2(t)}\right). \tag{2}$$

We apply the following assumptions to (1):

- **A1.** Convection from the part into the ambient air, $q_{\text{conv.}}$, and radiative heat transfer between the part and environment, $q_{\text{rad.}}$, are neglected because the Biot number for PBF is approximately Bi = 0.01 [33].
- **A2.** The loosely packed powder that surrounds the part is a poor conductor [34], therefore, conduction between the part and powder is negligible. This constructs a Neumann boundary condition at surfaces Γ , $\nabla T \cdot \hat{\mathbf{n}} = 0 \ \forall \ \mathbf{v} \in \Gamma$, as shown in Fig. 2, where $\nabla = \left(\frac{\partial}{\partial x}, \frac{\partial}{\partial y}, \frac{\partial}{\partial z}\right)$, \cdot is the vector dot product, and $\hat{\mathbf{n}}$ is the direction normal to the surface Γ .
- **A3.** We assume that the machine base plate is an ideal heat sink. Therefore, surfaces Λ have constant temperature T_0 , setting up the Dirichlet boundary condition $T = T_0 \ \forall \ \mathbf{v} \in \Lambda$ and t (Fig. 2).
- **A4.** The top layer is composed of fully-fused metal with a thermal conductivity equal to the bulk conductivity. This represents the assumption that new material added to the part is negligible in comparison to the volume of V, within the timescale of analysis. We invoke this assumption to better predict the controls-theoretic properties of our linear systems [32].

These assumptions sacrifice model accuracy to construct computationally efficient linear models, which we discuss in the next section. Incorporating the EnKF corrects for errors induced by these assumptions.

2.2 Model construction

The assumptions of Section 2.1 reduce (1) to (3), which is the well-known Fourier's Law of Conduction applied to V.

$$\frac{\partial T(\xi,t)}{\partial t} = \frac{k}{\rho c} \nabla^2 T(\xi,t) \,\forall \, \xi \in V$$

$$T(\xi,t) = T_0 \,\forall \, \xi \in \Lambda$$

$$\nabla \cdot T(\xi,t) = 0 \,\forall \, \xi \in \Gamma$$

$$\nabla \cdot T(\bar{\xi},t) = u(\bar{\xi},t) \,\forall \, \bar{\xi} \in \Omega.$$
(3)

We seek a numerical solution to (3), which begins by discretizing V into a collection of n nodes, $\xi_1, \xi_2, \ldots, \xi_n$, connected by edges and grouped into E elements. We define the *state vector*, $\mathbf{x}(t)$, as the temperature at all nodes, (4), and leverage the FEM theory of [35] to solve for these temperatures. The FEM solution to $\mathbf{x}(t)$ is governed by (5), where \mathbf{M} stores heat capacitance information, and \mathbf{K} stores thermal conductivity information. The FEM heat input function, $\mathbf{r}(t, u(\bar{\xi}, t))$, (6), depends on a set of *shape functions*, \mathbf{N}_e [35]. These distribute $u(\bar{\xi}, t)$ among the associated nodes of the element surface S_e .

$$\mathbf{x}(t) = [T(\xi_1, t), T(\xi_2, t), \dots, T(\xi_n, t)]' \in \mathbb{R}^n, \tag{4}$$

$$\dot{\mathbf{x}}(t) = \underbrace{\mathbf{A}\mathbf{x}(t)}_{\mathbf{A} = -\mathbf{M}^{-1}\mathbf{K}} + \mathbf{r}(t, u(\bar{\xi}, t)), \tag{5}$$

$$\mathbf{r}(t, u(\bar{\xi}, t)) = \mathbf{M}^{-1} \sum_{e=1}^{E} \int_{S_e} u(\bar{\xi}, t) \mathbf{N}_e(t)' dS_e.$$
 (6)

Constructing linear models from (5) is complex, and detailed in [32]. This process depends on whether we consider E-PBF (Fig. 1a) or L-PBF (Fig. 1b), because different input modes and measurement modes are available for each. The input modes govern the input-to-state relationship of the system, which models heat application. Mathematically, this is represented by replacing $\mathbf{r}(t,u(\bar{\xi},t))$ with $\mathbf{B}(t)\mathbf{u}(t)$, where $\mathbf{B}(t)$ and $\mathbf{u}(t)$ are to be defined. The measurement modes govern the state-to-output relationship of the system, which models IR cameras measuring temperatures on Ω . Mathematically, this is represented by constructing an output equation, $\mathbf{y}(t) = \mathbf{C}(t)\mathbf{x}(t)$, where $\mathbf{y}(t)$ and $\mathbf{C}(t)$ are to be defined.

2.2.1 Input modes

The E-PBF electron beam is capable of rastering atop the part so fast that it produces an arbitrary heat flux on Ω , as shown in Input 1 of Fig. 1a. The engineer may apply an arbitrary (non-negative) flux to any subset of regions in Ω at any time by moving the beam sufficiently quickly. In reflection of this ability, we let $\mathbf{u}(t) \in \mathbb{R}^m$ be the values of $u(\bar{\xi},t)$ at the centroids of all m FEM elements with faces on Ω . All components of $\mathbf{u}(t)$ can change independently of the others, which models the arbitrary flux on Ω . This constructs a linear, time-invariant (LTI) input-to-state

relationship, $\mathbf{r}(t, u(\bar{\xi}, t)) \approx \mathbf{B}\mathbf{u}(t)$, where **B** distributes the fluxes of $\mathbf{u}(t)$ among the nodes of their respective elements.

The L-PBF laser cannot generate an arbitrary heat flux like the E-PBF electron beam. Instead, we must linearize $\mathbf{r}(t, u(\bar{\xi}, t))$ with respect to any selection of Inputs 1-4, as shown in Fig. 1b. In this work, as in [32], we select Inputs 1 and 2, denoting this input as $\mathbf{u}_1(t) = [P(t), r_b^2(t)]'$. In this scheme, the laser moves along a predefined trajectory and the engineer only controls the laser characteristics as it moves. $x_c(t)$ and $y_c(t)$ are treated as time-varying parameters of $\mathbf{r}(t, \mathbf{u}_1(t))$. We choose an operating point, $\mathbf{u}_0 = [P_0, r_{b,0}^2]'$, and linearize $\mathbf{r}(t, \mathbf{u}_1(t))$ to obtain $\mathbf{r}(t, \mathbf{u}_1(t)) \approx \mathbf{r}(t, \mathbf{u}_0) + \mathbf{B}(t)\delta\mathbf{u}(t)$, where $\delta\mathbf{u}(t) = [\delta P(t), \delta r_b^2(t)] = \mathbf{u}(t) - \mathbf{u}_0$. We show in [32] that $\mathbf{r}(t, \mathbf{u}_0) = \mathbf{B}(t)[P_0, 0]'$, therefore $\mathbf{r}(t, \mathbf{u}_1(t)) \approx \mathbf{B}(t)\mathbf{u}(t)$, where $\mathbf{B}(t)$ follows from the linearization procedure and $\mathbf{u}(t) = [P(t), \delta r_b^2(t)]'$.

2.2.2 Measurement modes

We model E-PBF machines that have an infrared (IR) camera measuring temperatures on Ω as the system output (Measurement 2, Fig. 1a). This camera is assumed to have P pixels, arranged in a grid, which all record $T(\bar{\xi},t)$ at fixed locations in Ω , each denoted by a coordinate pair, (x_i,y_i) . $\mathbf{y}(t) \in \mathbb{R}^p$ collects the measured temperature signals at a set of p pixels from the P-pixel grid, using methodologies explained in Section 3.2. We interpolate the signal at each component of $\mathbf{y}(t)$, $\mathbf{y}_i(t)$, from the nodes of $\mathbf{x}(t)$ on Ω . For such a node on Ω with coordinates $(x_{j,\mathbf{x}},y_{j,\mathbf{x}})$, the weighting coefficient is $\mathbf{C}_{ij} = \exp\left(-((x_i-x_{j,\mathbf{x}})^2+(y_i-y_{j,\mathbf{x}})^2)/\sigma^2\right)$, where σ is the pixel spacing in the grid. For all nodes not on Ω , $\mathbf{C}_{ij} = 0$. \mathbf{C} collects all such weights, with all entries being divided by the sum of their respective rows, to form the state-to-output relationship $\mathbf{y}(t) = \mathbf{C}\mathbf{x}(t)$.

L-PBF machines can be equipped with two IR cameras: an IR camera that images all of Ω similarly to E-PBF machines (Measurement 2, Fig. 1b), and a coaxial IR camera that images the melt pool with very high resolution (Measurement 3, Fig. 1b). For L-PBF, We consider Measurement 3 to be the system output, $\mathbf{y}(t) \in \mathbb{R}^p$, with p being the number of selected pixels in the camera field of view (FOV) (Section 3.2). We construct the L-PBF state-to-output relationship with the same interpolation scheme as E-PBF. However, for Measurement 3, the location of each pixel, $(x_i(t), y_i(t))$, is time-varying as the camera FOV moves with the laser. The resulting non-zero weights, $\mathbf{C}_{ij}(t)$, become time-varying, which produces the time-varying state-to-output relationship $\mathbf{y}(t) = \mathbf{C}(t)\mathbf{x}(t)$. An additional concern of Measurement 3 is laser turnaround. As elaborated in Section 3.1, our simulated laser (and e-beam) trajectories incorporate *skywriting*, a common industry practice where the heat source turns around while outside the part domain. We preserve simulated image quality during skywriting as follows: If the pixel coordinate $(x_i(t), y_i(t))$ is within Ω , we divide all entries of the row \mathbf{C}_i by the row sum. If not, no division is performed.

We generate two linear systems from these constructions, which are shown below.

E-PBF:
$$\dot{\mathbf{x}}(t) = \mathbf{A}\mathbf{x}(t) + \mathbf{B}\mathbf{u}(t) \\
\mathbf{y}(t) = \mathbf{C}\mathbf{x}(t),$$
(7)

L-PBF:
$$\dot{\mathbf{x}}(t) = \mathbf{A}\mathbf{x}(t) + \mathbf{B}(t)\mathbf{u}(t) \\
\mathbf{y}(t) = \mathbf{C}(t)\mathbf{x}(t).$$
(8)

Equations (5), (7), and (8) are expressed in discrete time by letting $\dot{\mathbf{x}}(t_{k+1}) = \Delta t^{-1}(\mathbf{x}(t_{k+1}) - \mathbf{x}(t_k))$, where $t_k = k\Delta t$ for k = 0, 1, 2, ..., and $\Delta t > 0$ is the simulation time step.

2.3 EnKF algorithm

The estimations of models (7)-(8) are corrected with Algorithm 1, which we adapt from the EnKF algorithm of [31]. In Algorithm 1, \mathbf{B}_k and \mathbf{C}_k denote $\mathbf{B}(t_k)$ and $\mathbf{C}(t_k)$, as applicable. Algorithm 1 implements N Kalman filters in parallel, which generate N state estimate signals and sensor measurements, which we group into \mathbf{X}_k (the *ensemble*) and \mathbf{Y}_k , respectively. Using \mathbf{X}_k and \mathbf{Y}_k , we generate sample estimates of the estimation error and measurement noise covariances.

 \mathbf{W}_k in Algorithm 1 simulates process noise being injected into each of the N systems of the algorithm. This noise captures random perturbations to the PBF thermal dynamics like turbulent flow in the melt pool or spatter ejection. In Algorithm 1, we let $\mathbf{W}_k = [\mathbf{w}_k^1, \mathbf{w}_k^2, \dots, \mathbf{w}_k^N]$, where all $\mathbf{w}_k^i \sim \mathcal{N}(\mathbf{0}, \mathbf{I})$ are independent, identically-distributed (IID) Gaussian random vectors. This construction lets us simulate the random effects of N PBF processes simultaneously, without needing N physical machines.

The EnKF requires N measurements of the system. In place of collecting data from N physical sensors, as is typically done in EnKF literature, we take a singular measurement, $\mathbf{y}_{FEM}(t_k)$, and copy it N times, $\mathbf{y}_{FEM}(t_k)\mathbf{1}_{1\times N}$. We then corrupt these copies with independent instances of white noise, \mathbf{V}_k . Similarly to \mathbf{W}_k , \mathbf{V}_k represents $\mathbf{y}_{FEM}(t_k)$ being collected synchronously by multiple identical sensors, with each reading being corrupted by random perturbances like electronic noise. We model \mathbf{V}_k as $\mathbf{V}_k = [\mathbf{v}_k^1, \mathbf{v}_k^2, \dots, \mathbf{v}_k^N]$, where all $\mathbf{v}_k^i \sim \mathcal{N}(\mathbf{0}, \mathbf{I})$ are IID Gaussian random vectors.

Algorithm 1 requires no *a priori* knowledge of the true process and measurement noise distributions to function. If the true distributions differ from those used to construct \mathbf{W}_k and \mathbf{V}_k , Algorithm 1 generates $\bar{\mathbf{P}}_{k|k-1}$ and $\bar{\mathbf{R}}_{k|k-1}$ that represents the combination of the true and assumed distributions. The closer the assumed distributions match reality, the smaller N can be without sacrificing filter accuracy.

As shown in Algorithm 1, we apply *localization* to the estimated state covariance, $\bar{\mathbf{P}}_{k|k-1}$. Localization mitigates the tendency for $\bar{\mathbf{P}}_{k|k-1}$ to produce overly-aggressive correlations between the thermal responses of nodes that are far apart. This error is an artifact of a finite sample size, N. Standard localization techniques, [36], reduce these artificially-high components of $\bar{\mathbf{P}}_{k|k-1}$, $\bar{\mathbf{P}}_{ij}$, via the construction $\bar{\mathbf{P}}_{k|k-1} \leftarrow \mathbf{F} \circ \bar{\mathbf{P}}_{k|k-1}$, where $\mathbf{F}_{ij} = \exp\left(-\frac{l_{ij}^2}{L^2}\right)$. l_{ij}^2 is the Cartesian distance

Initialization

 $\hat{\mathbf{X}}_0 \in \mathbb{R}$, initial state ensemble

 $\hat{\mathbf{x}}_{0|0}$, initial state estimate

while Not end of runtime do

Predict

 $\mathbf{X}_k = \mathbf{A}\mathbf{X}_{k-1} + \mathbf{B}_k\mathbf{u}_k\mathbf{1}_{1\times N} + \mathbf{W}_k$, propagate state ensemble

 $\cdot \mathbf{Y}_k = \mathbf{y}_{FEM}(t_k)\mathbf{1}_{1\times N} + \mathbf{V}_k$, generate measurement ensemble $\cdot \bar{\mathbf{x}} = N^{-1}\mathbf{X}_k\mathbf{1}_{N\times 1}, \ \bar{\mathbf{y}} = N^{-1}\mathbf{Y}\mathbf{1}_{N\times 1}$ compute ensemble averages $\cdot \bar{\mathbf{P}}_{k|k-1} = (N-1)^{-1}(\mathbf{X}_k - \bar{\mathbf{x}}\mathbf{1}_{1\times N})(\mathbf{X}_k - \bar{\mathbf{x}}\mathbf{1}_{1\times N})'$,

 $\bar{\mathbf{R}}_{k|k-1} = (N-1)^{-1} (\mathbf{Y}_k - \bar{\mathbf{y}} \mathbf{1}_{1 \times N}) (\mathbf{Y}_k - \bar{\mathbf{y}} \mathbf{1}_{1 \times N})'$, compute ensemble covariances

 $\cdot \mathbf{\bar{P}}_{k|k-1} \leftarrow \mathbf{F} \circ \mathbf{\bar{P}}_{k|k-1}$, Apply localization

 $\cdot \tilde{\mathbf{Y}}_k = \mathbf{Y}_k - \mathbf{C}_k \mathbf{X}_k$, compute ensemble innovation

 $\cdot \bar{\mathbf{S}}_{k|k-1} = \mathbf{C}_k \bar{\mathbf{P}}_{k|k-1} \mathbf{C}_k' + \bar{\mathbf{R}}_{k|k-1}$, compute ensemble innovation covariance $\cdot \mathbf{K}_k = \bar{\mathbf{P}}_{k|k-1} \mathbf{C}_k' \bar{\mathbf{S}}_{k|k-1}^{\dagger}$, compute Kalman gain

 $\hat{\mathbf{X}}_k = \mathbf{X}_k + \mathbf{K}_k \tilde{\mathbf{Y}}_k$, compute updated ensemble

 $\hat{\mathbf{x}}_{k|k} = N^{-1}\hat{\mathbf{X}}_k\mathbf{1}_{N\times 1}$, compute EnKF estimate

 $\hat{\mathbf{y}}_{k|k} = \mathbf{C}_k \hat{\mathbf{x}}_{k|k}$, compute Kalman output estimate

end

Algorithm 1: Ensemble Kalman Filter. [†] denotes pseudoinversion. ○ denotes the Schur product.

between nodes i and j, and L is an arbitrary hyperparameter that represents the characteristic length of the system. We adapt this approach in two ways. First, as shown in (9), we let $L = 2\sqrt{\alpha \Delta t}$, the thermal diffusion length of the system [37]. Second, we do not consider l_{ij} when penalizing distance between nodes i and j. As shown in Fig. 3, using the Cartesian distance could construct a thermal path that leads through the powder, which we model as insulation (Assumption A.2). Instead, we compute the exponential argument of (9), d_s , for all edges in the mesh. l_s is the Cartesian length of a given edge in the mesh, and α_s for each edge is averaged from the α of all elements containing that edge. Treating all \mathbf{d}_s as edge weights, we compute the shortest weighted distance between nodes i and j, as shown in Fig. 3, and use it to calculate \mathbf{F}_{ij} , (9).

$$\mathbf{F}_{ij} = \exp\left(-\sum_{\text{shortest path}} \underbrace{\frac{l_s^2}{4\alpha_s \Delta t}}_{d_s}\right) \tag{9}$$

3 Test procedures

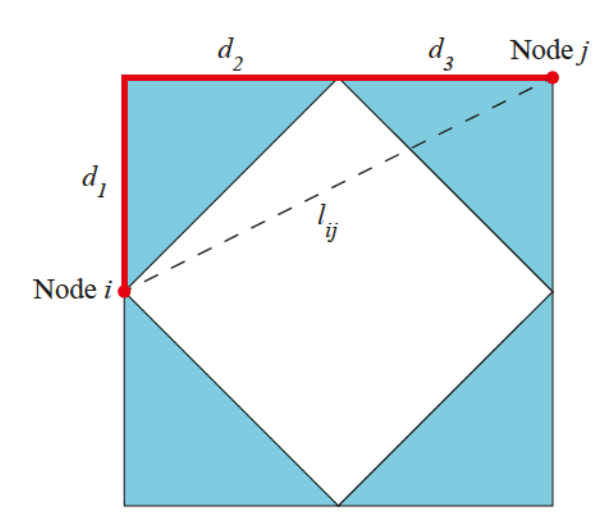


Figure 3: Demonstration of computing the exponential argument of (9). The red line shows the shortest thermal path between nodes i and j, consisting of three edges. The white space represents powder. The dotted black line represents the cartesian distance between nodes i and j, l_{ij} .

System $K [W^1m^{-1}K^{-1}]$ $c [J^1kg^{-1}K^{-1}]$ $\rho [kg^1m^{-3}]$ (5) 16 500 7920 (7)-(8) 24 640 8070

Table 1: Material properties sets

3.1 Test parameters

For all tests, we generate (5), (7), and (8) from the mesh geometry of Fig. 4 and the material properties listed in Table 1. The material properties of System (5) represent 304 stainless steel (SS) at low temperature, and those of Systems (7)-(8) represent 304 SS at elevated temperature [38]. In doing so, we test the ability of Algorithm 1 to compensate for systemic uncertainty in the system structure. All tests last 5514 time steps, with $\Delta t = 0.0001$ s.

For all tests, the heat source, (2), moved according to the following trajectory, with $x_c(t)$ and $y_c(t)$ in meters

$$x_c(t) = 0.01t$$

 $y_c(t) = 0.0075 \sin(\underbrace{253.33}_{f}t) + 0.0025.$ (10)

 $y_c(t)$ in (10) corresponds to a laser that oscillates in the y-direction to a maximum of 5 mm beyond the part boundary in either direction. The oscillation frequency is defined as $f = 2v_y/0.0075$, where $v_y = 0.95$ m/s represents the nominal speed. We let P(t) of (2) be $P(t) = P_{\text{nom}} = 250$ W

when the heat source is overtop Ω ($0 \le y_c(t) \le 0.005$ m), and 0 W otherwise. For all tests involving System (7), we let $r_b(t) = 40 \ \mu\text{m} \ \forall \ t \ge 0$ when constructing Systems (5) and (7). For all tests involving System (8), we let $r_{b,0} = 40 \ \mu\text{m}$ when constructing System (8) and $P_0 = P_{\text{nom}}$, but let $r_b(t) = 50 \ \mu\text{m} \ \forall \ t \ge 0$ when constructing System (5). We do this because System (8) anticipates that there is uncertainty between the nominal and actual values of $r_b(t)$.

To construct $\mathbf{y}(t)$ of Systems (7)-(8), we define two virtual IR cameras, mimicking Measurements 2-3 of Fig. 1. We simulate the camera of Measurement 2 with a 75 x 34 grid of pixels, with a FOV that covers all of Ω . 75 pixels span the x-axis of Ω of Fig. 4, and 34 pixels span the y-axis. We simulate the camera of Measurement 3 with a 50 x 50 grid of pixels that surround the laser centerpoint, comprising a 0.324 mm x 0.324 mm FOV. We simulate collecting data with these cameras by interpolating temperatures on Ω onto the pixel grids, as explained in Section 2.2.2. Measurements 2 and 3 are constructed from these cameras by selecting pixels at random to be part of the measurement (system output), as explained in the next section. For all tests, the state-to-output relationship of System (5) is the same as the

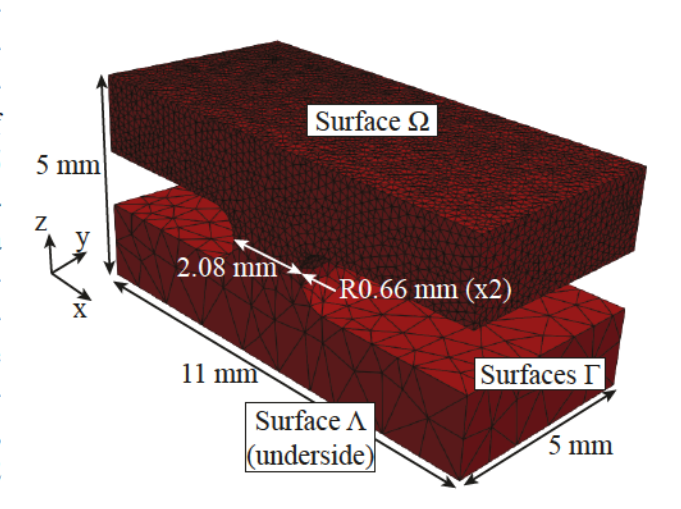


Figure 4: FEM mesh used to conduct all tests, with all geometric features dimensioned. The mesh consists of 33,882 nodes and 186,400 elements.

corresponding linear system, System (7) or (8), as applicable.

3.2 Testing schedule

Table 2 summarizes the tests we conduct in this work. Each numbered test of Table 2 has three parts: part a (test 1a, test 2a, etc.), which runs the test on System (7), and parts b and c (test 1b, test 2b, test 1c, etc.), which run the tests on System (8). For each triplet of tests, a portion of the pixels from the cameras comprising Measurements 2 and 3, as applicable, are selected at random. Table 2 lists the amount of selected pixels for each test, p, and the distribution the pixels were drawn from. Figs. 5-6 show the selected pixels. This test schedule represents measuring Ω with IR cameras that are increasingly inexpensive and feature lesser computational burden, but measure increasingly less information.

The pixels for tests a and tests b are selected with Poisson disk sampling (PDS), [39], to help ensure they are distributed evenly throughout the camera FOV as p decreases, as shown in Figs. 5-6. Our procedure for doing so is shown in Fig. 8. PDS returns a set of points within the specified FOV, required to be mutually distant by at least a selected magnitude, but otherwise chosen at random. These points need not be coincident with the locations of the camera pixels. For each successive PDS point, we associate with it the closest pixel in the camera FOV that has not yet been associated with a previous point. These pixels define our output signal, $\mathbf{y}(t)$ =

System	Test number					
	Pixel count, p , and pixel distribution					
	Test letter	1	2	3	4	5
(7)		211	29	27	2 ⁵	2 ³
	a	PDS	PDS	PDS	PDS	PDS
(8)		2^{11}	2^{9}	2^7	2^5	2^3
	b	PDS	PDS	PDS	PDS	PDS
	c	Gauss	Gauss	Gauss	Gauss	Gauss

 $[\mathbf{y}_1(t), \mathbf{y}_2(t), \dots, \mathbf{y}_p(t)]'$, as described in Section 2.2.2.

By prioritizing an even distribution of selected pixels, we avoid bias in our results that would appear if we attempted optimizing the pixel locations with respect to filter accuracy. We assess the impact of this bias in tests c, where we select p pixels about the FOV center of Measurement 3 via the Gaussian distribution (Fig. 6). This distribution has a variance of 70 μ m. We hypothesize that concentrating our measurements about the hottest region of the melt pool, the center of Measurement 3, will yield more accurate results than selecting pixels evenly about the FOV.

For each test, performance is quantified with the following set of error signals

Error 2-norms:
$$\begin{cases} \tilde{\mathbf{x}}_{2,EnKF}(t_k) = ||\mathbf{x}_{FEM}(t_k) - \hat{\mathbf{x}}_{k|k}||_2 \\ \tilde{\mathbf{x}}_{2,OL}(t_k) = ||\mathbf{x}_{FEM}(t_k) - \mathbf{x}_{OL}(t_k)||_2 \end{cases}$$
 Error ∞ -norms:
$$\begin{cases} \tilde{\mathbf{x}}_{\infty,EnKF}(t_k) = ||\mathbf{x}_{FEM}(t_k) - \hat{\mathbf{x}}_{k|k}||_{\infty} \\ \tilde{\mathbf{x}}_{\infty,OL}(t_k) = ||\mathbf{x}_{FEM}(t_k) - \mathbf{x}_{OL}(t_k)||_{\infty}. \end{cases}$$

Here, $\mathbf{x}_{FEM}(t_k)$ is the solution to System (5), $\mathbf{x}_{OL}(t_k)$ is the solution to Systems (7)-(8), and $\hat{\mathbf{x}}_{k|k}$ is the solution returned by Algorithm 1. To compare the relative magnitude of these error signals, we take the norms of these norms:

2-norms of 2-norms:
$$\begin{cases} ||\tilde{\mathbf{x}}_{2,EnKF}(t_k)||_2\\ ||\tilde{\mathbf{x}}_{\infty,OL}(t_k)||_{\infty} \end{cases}$$

$$\infty\text{-norms of }\infty\text{-norms:} \begin{cases} ||\tilde{\mathbf{x}}_{\infty,EnKF}(t_k)||_{\infty}\\ ||\tilde{\mathbf{x}}_{\infty,OL}(t_k)||_{\infty}. \end{cases}$$

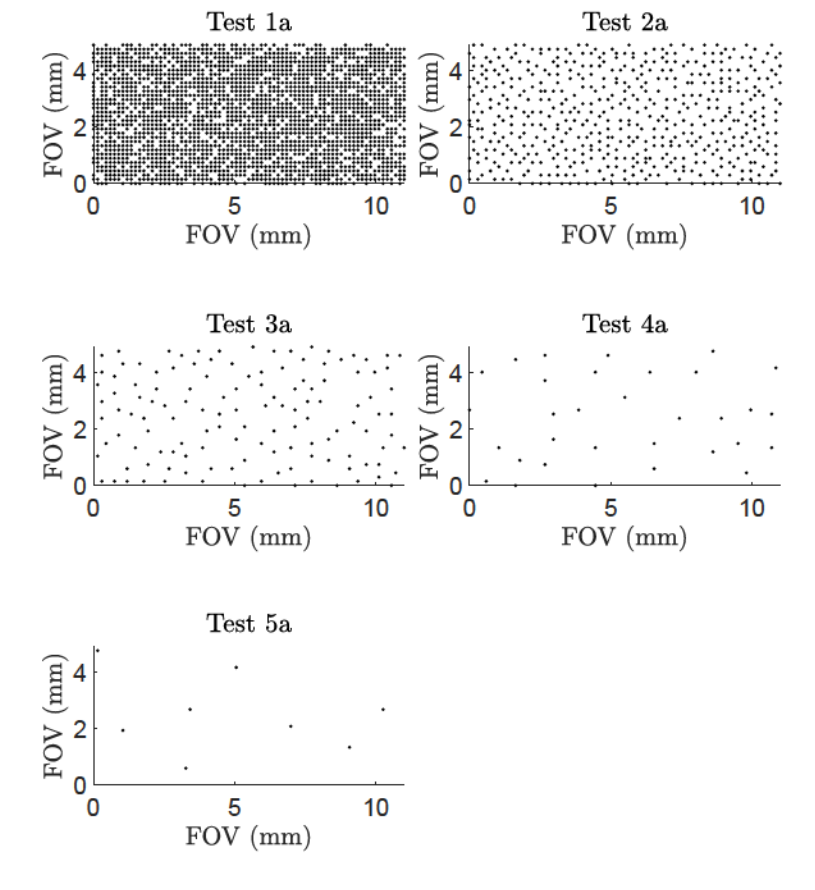


Figure 5: Location of selected pixels for y(t) of System (7), based on Measurement 2 of Fig. 1a, as described in Table 2.

We find it convenient to normalize these norms-of-norms values, and introduce additional notation to denote the normalized values:

$$\begin{aligned} ||\hat{\mathbf{e}}||_2 &= ||\tilde{\mathbf{x}}_{2,EnKF}(t_k)||_2 / ||\tilde{\mathbf{x}}_{2,OL}(t_k)||_2 \\ ||\hat{\mathbf{e}}||_{\infty} &= ||\tilde{\mathbf{x}}_{\infty,EnKF}(t_k)||_{\infty} / ||\tilde{\mathbf{x}}_{\infty,OL}(t_k)||_{\infty} \end{aligned}$$

4 Results

The results of Tests 1-5 are summarized in Fig. 7. Our points of discussion are as follows: Fig. 7 reveals a lesser magnitude of $||\hat{\mathbf{e}}||_2$ System (8) than (8) for all p. Even more critically, System (8) features diminishing returns in filter accuracy (reduction of $||\hat{\mathbf{e}}||_2$) with respect to increasing p, and System (7) does not. Finally, tests c produces inferior results (larger $||\hat{\mathbf{e}}||_2$ and $||\hat{\mathbf{e}}||_{\infty}$) than test b. The remainder of this section discusses these points in detail.

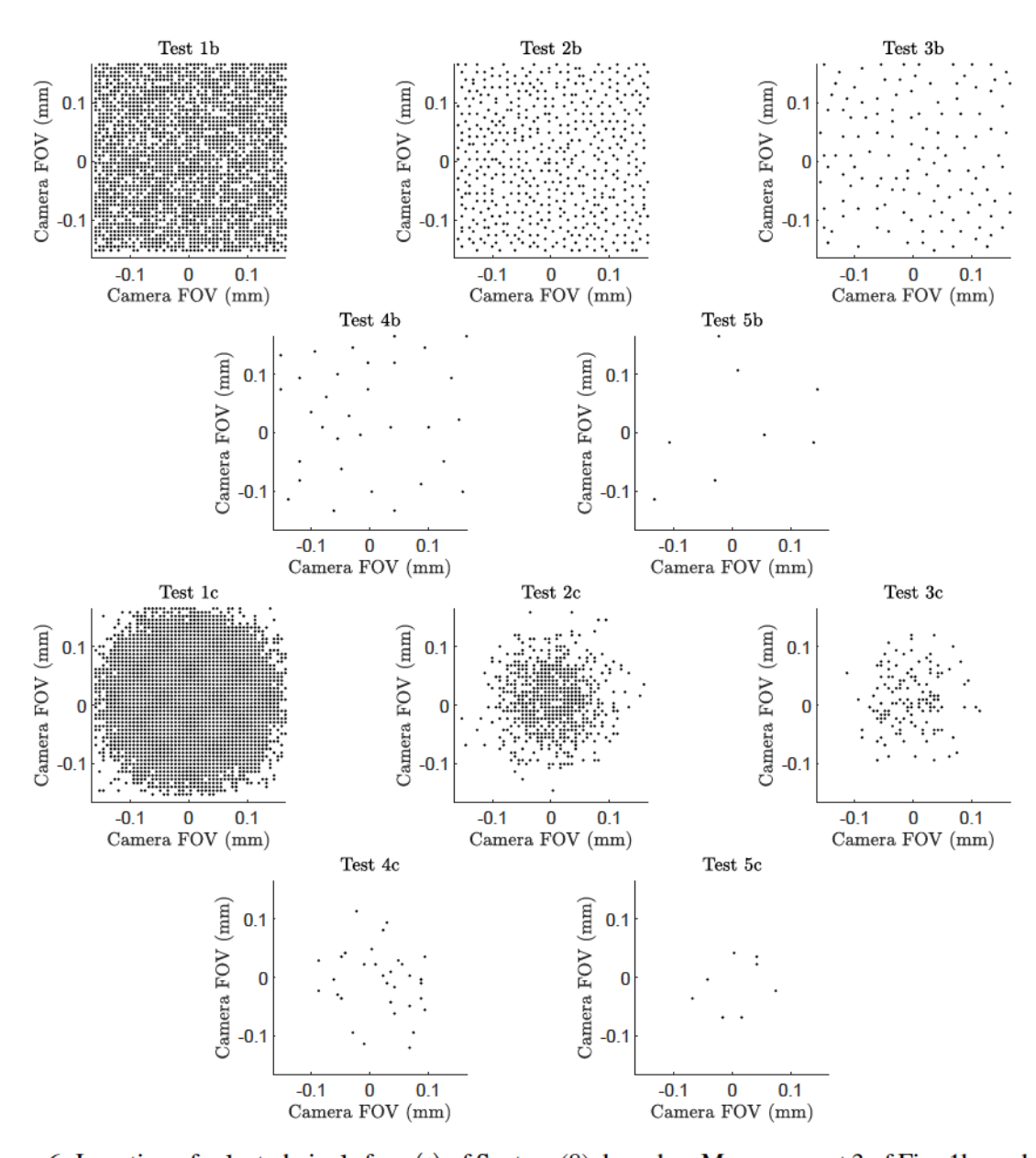


Figure 6: Location of selected pixels for y(t) of System (8), based on Measurement 3 of Fig. 1b, as described in Table 2.

4.1 Analysis of $\tilde{\mathbf{x}}_2(t_k)$, $||\hat{\mathbf{e}}||_2$, tests a and b

We begin by analyzing the filter 2-norm error, which the EnKF minimizes [31], as a function of p. We first consider tests a and b. We observe from 7 that $||\hat{\mathbf{e}}||_2$ for tests b is uniformly higher than that of tests a, up to a 3x improvement. We attribute this improvement to the fact that Measurement 3 is much more detailed near the melt pool than Measurement 2. As explained in Section 3.1, the pixel resolution of Measurement 2 is approximately 133 μ m, and that of Measurement 3 is approximately 6.48 μ m. Thus, Measurement 3 collects much more detailed information about $T(\bar{\xi},t)$ near the heat source than Measurement 2, where $T(\xi,t)$ displays the most extreme

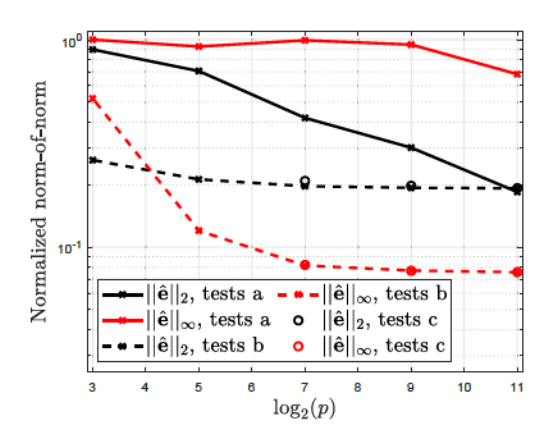


Figure 7: Norms of error norms vs pixel count, p, for all tests.

gradients. Detailed measurements of these gradients are more important than the more extensive far-afield measurements provided by Measurement 2, and thus yield better filter performance. The discrepancy grows as *p* decreases, which increases the effective pixel spacing for both tests, which produces the increasing relative improvement of tests b shown in Fig. 7.

Crucially, we observe that $||\hat{\mathbf{e}}||_2$ decays in magnitude as p increases for tests b. means that System (8) exhibits diminishing returns in filter accuracy as camera resolution increases, as measured by the diminishing reduction in $||\hat{\mathbf{e}}||_2$. Increasingly-dense (and expensive) camera measurements do not necessarily translate into meaningful performance improvements. However, unlike $||\hat{\mathbf{e}}||_2$ of tests b, $||\hat{\mathbf{e}}||_{\infty}$ of tests a does not reach an asymptote. This is because the coaxial camera of tests b captures no information far afield of the melt pool. Even with an infinitely-dense pixel array within the camera FOV, not having this information constrains the filter's accuracy. Since the global camera of tests a images all of Ω , performance always improves as p increases.

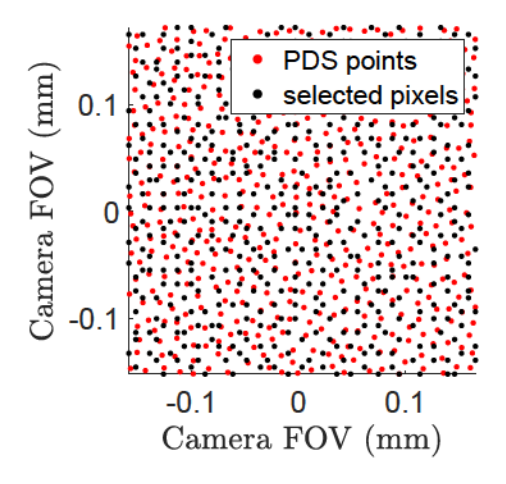


Figure 8: Selection of pixels corresponding to the points returned by the PDS algorithm, using the configuration of Test 2b (Table 2) as an example.

As demonstrated in Fig. 9, spikes in $\tilde{\mathbf{x}}_2(t_k)$ are a large contributor to $||\hat{\mathbf{e}}||_2$. This is particularly true for tests b. Fig. 9 shows $\tilde{\mathbf{x}}_2(t_k)$ displays a relatively constant error floor, with improvements in $||\hat{\mathbf{e}}||_2$ deriving chiefly from reducing the magnitude of spikes above this floor. We attribute the asymptote of $||\hat{\mathbf{e}}||_2$ for tests b to the invariance of the error floor magnitude. Identifying the cause of these error spikes, to more effectively reduce their magnitude, is a matter of ongoing research.

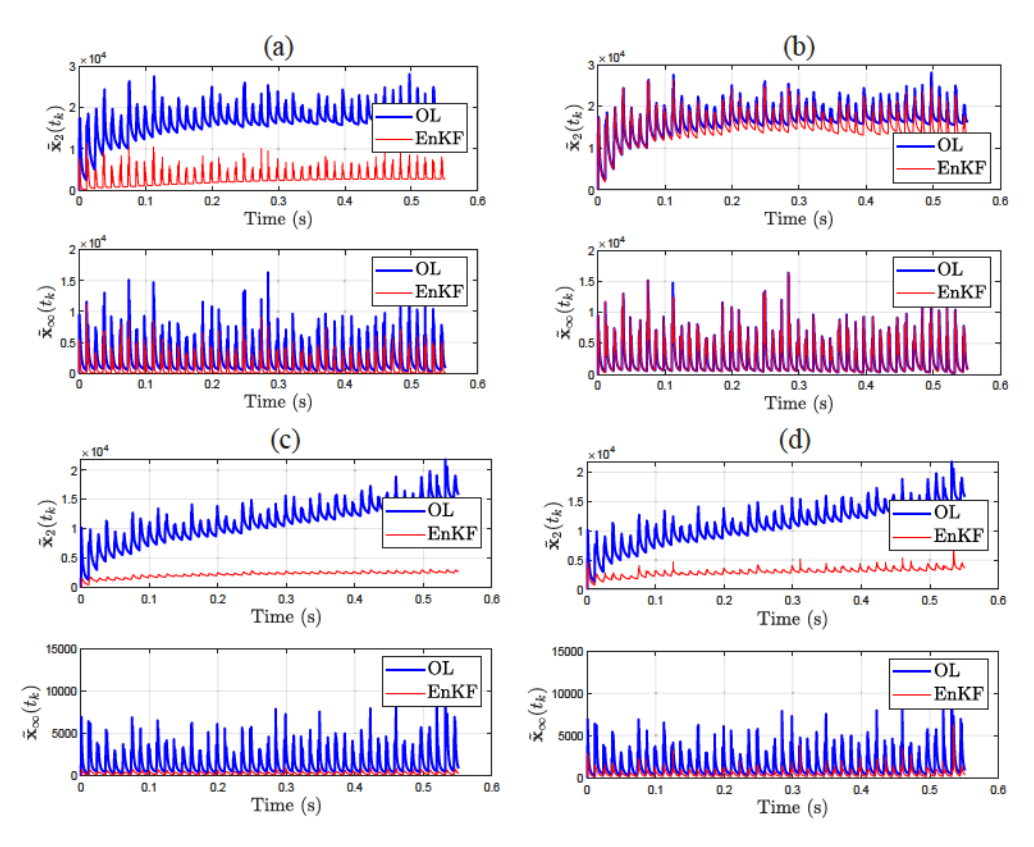


Figure 9: $\tilde{\mathbf{x}}_2(t_k)$ and $\tilde{\mathbf{x}}_{\infty}(t_k)$ for selected tests: (a) Test 1a, (b) Test 5a, (c) Test 1b, (d) Test 5b

4.2 Comparison of performance of tests b and c

As shown in Fig. 7, $||\hat{\mathbf{e}}||_2$ and $||\hat{\mathbf{e}}||_\infty$ for tests c is comparable to those of tests b for $p \ge 128$, after which the relative performance degrades. This refutes our earlier hypothesis that tests c would exhibit superior performance than tests b. We believe this is because the clustered measurements do not adequately capture temperature gradients from the melt pool peak to the peripheral of the heat affected zone (HAZ). Letting the variance of the Gaussian distribution approximate the beam diameter (Section 3) means the majority of selected pixels measure near-peak temperatures. Especially for small p, few pixels are selected at far enough distances from the laser center to measure temperatures within the greater HAZ. Under these conditions, the filter struggles to estimate temperature gradients within the HAZ, and therefore exhibits inferior accuracy. As p increases, the number of pixels within the greater HAZ increases, and Fig. 7 reflects the enhanced performance of the filter. Beyond this discrepancy, the overall behavior of tests c is similar to that of tests b, and the conclusions drawn about the behavior of tests b apply similarly. We conjecture that truly optimal pixel distributions for extremely low p would resemble cross-shaped patterns that span the entirety of the FOV.

5 Conclusions

In this work, we apply an Ensemble Kalman Filter (EnKF) [31] to the problem of estimating internal temperature distributions within parts being built by the Powder Bed Fusion (PBF) process. The algorithm synthesizes models of the problem physics and in-situ process measurements to correct for modeling inaccuracies without needing extensive training data. We adapt the EnKF algorithm to make it more applicable to PBF thermal domains, and test the algorithm efficacy in simulation. Our simulation tests consider linear 3D part models of two different configurations, which model electron beam PBF (E-PBF) and laser PBF (L-PBF) heat transfer with the finite element method. Our "in-situ" process measurements are simulated thermal cameras with a varying amount of pixels, denoted *p*. Each model configuration uses a different simulated camera type, in reflection of the differing hardware constraints on L-PBF and E-PBF. The simulated cameras take measurements from a more accurate, nonlinear, process model than those used to construct the EnKF, which also is constructed using different material properties. We compare algorithm efficacy for both model configurations as a function of *p*.

Our most important result is that the EnKF, applied to the L-PBF model configuration, features diminishing returns in 2-norm accuracy improvement as p increases, reaching a horizontal asymptote of roughly 81% error reduction. The L-PBF configuration utilizes a coaxial infrared camera, as is standard in PBF process monitoring. Diminishing accuracy improvements with respect to increasing p means coaxial cameras with high pixel densities do not yield correspondingly superior results relative to coaxial cameras with coarser resolutions. Process engineers seeking to employ coaxial cameras in their quality control strategies need not incur the expense and computational difficulties of high-resolution cameras. Appropriately-designed algorithms allow coaxial cameras with coarser resolutions, which are cheaper and feature easier-to-process data streams, to achieve equivalent results. Our tests show that 2-norm accuracy for E-PBF configurations, which use off-axis cameras, does not reach an asymptote. However, the poor resolution of these cameras means resolving the melt pool would require extremely high p, which would be computationally impractical.

We show that filter accuracy is better when measurements are taken from pixels scattered uniformly throughout the camera field of view (FOV), instead of measuring from pixels clustered about the FOV center, when testing with the L-PBF configuration. This result indicates that process engineers who are interested in optimal PBF temperature estimation should take measurements at the peripheral of the heat affected zone in addition to measurements of the melt pool center.

Our tests also show that the L-PBF model configuration yields more accurate EnKF estimations than the E-PBF configuration, relative to their respective model predictions in the absence of the filter, for all p. We believe this is because the camera available to L-PBF is trained on the melt pool with very high resolution, whereas the E-PBF camera primarily captures far-afield temperatures and lacks the resolution to image the melt pool clearly. The melt pool provides the most useful information about PBF thermal dynamics, which results in the EnKF providing superior results when using data from the L-PBF camera. We believe this difference explains why the ∞ -norm accuracy of the filter for the E-PBF configuration is relatively invariant to p when p is small.

Critically, this performance is obtained in the absence of the extensive libraries of training data that are usually required for PBF temperature field estimation algorithms. We do not believe that this algorithm will completely eliminate the need for training, but we anticipate that continuing to refine our approach will greatly reduce this burden while still offering good results.

Several avenues of research follow from this work. First, we are planning to collect experimental data so that we can test EnKF accuracy outside of simulation. We also intend to assess the improvements in filter accuracy if we synthesize data from multiple cameras into our measurements. The model configurations presented in this work incur large computational expense, which could be eliminated with the incorporation of adaptive meshing techniques. Estimation algorithms like the EnKF are necessary to apply control theory-based feedback control algorithms, the efficacy of which must be tested. Ultimately, this research represents progress towards making PBF quality control as independent of expensive training data as possible, which we believe delivers significant value to the industry.

References

- [1] N. Wood, E. Schwalbach, A. Gillman, and D. Hoelzle, "The ensemble kalman filter as a tool for estimating temperatures in the powder bed fusion process," in *American Control Conference 2021*, New Orleans, LA, USA, May 2021.
- [2] S. Ridwan, J. Mireles, S. Gaytan, D. Espalin, and R. Wicker, "Automatic layerwise acquisition of thermal and geometric data of the electron beam melting process using infrared thermography," in *Proceedings of the Annual International Solid Freeform Fabrication Symposium*, Austin, TX, USA, 2014, pp. 343–352.
- [3] R. Kleer and F. Piller, "Local manufacturing and structural shifts in competition: Market dynamics of additive manufacturing," *International Journal of Production Economics*, vol. 216, pp. 23–34, 2019.
- [4] R. Jiang, R. Kleer, and F. Piller, "Predicting the future of additive manufacturing: A delphi study on economic and societal implications of 3d printing for 2030," *Technological Fore-casting and Societal Change*, vol. 117, pp. 84–97, 2017.
- [5] A. McWilliams, "Chapter 7: Global markets for 3d printing (mfg074a)," BBC Research LLC, 2019 Manufacturing Research Review, Tech. Rep. MFG071B, 2019.
- [6] A. Wilson-Heid, S. Qin, and A. Beese, "Anisotropic multiaxial plasticity for laser powder bed fusion additively manufactured ti-6al-4v," *Materials Science & Engineering A*, vol. 738, pp. 90–97, 2018.
- [7] S. Karnati, A. Khiabhani, A. Flood, F. Liou, and J. Newkirk, "Anisotropy in impact toughness of powder bed fused aisi 304l stainless steel," *Material Design & Processing Communications*, vol. e59, 2019. [Online]. Available: https://doi.org/10.1002/mdp2.59

- [8] M. Liu, T. Wada, A. Suzuki, N. Takata, M. Kobashi, and M. Kato, "Effect of annealing on anisotropic tensile properties of al-12%si alloy fabricated by laser powder bed fusion," *Crystals*, vol. 10, no. 1007, 2020.
- [9] D. Agius, K. Kourousis, and C. Wallbrink, "A review of as-built slm ti-6al-4v mechanical properties towards achieving fatigue resistant designs," *Metals*, vol. 8, no. 75, 2018.
- [10] T. Becker, N. Dhansay, G. Ter Haar, and K. Vanmeensel, "Near-threshold fatigue crack growth rates of laser powder bed fusion produced ti-6al-4v," *Acta Materialia*, vol. 197, pp. 269–282, 2020.
- [11] A. Salmi and E. Atzeni, "Residual stress analysis of thin alsi10mg parts produced by laser powder bed fusion," *Virtual and Physical Prototyping*, vol. 15, no. 1, pp. 49–61, 2019.
- [12] R. Williams, C. Davies, and P. Hooper, "A pragmatic part scale model for residual stress and distortion prediction in powder bed fusion," *Additive Manufacturing*, vol. 22, pp. 416–425, 2018.
- [13] J. Bartlett and X. Li, "An overview of residual stresses in metal powder bed fusion," *Additive Manufacturing*, vol. 27, pp. 131–149, 2019.
- [14] M. Tang, C. Pistorius, and J. Beuth, "Prediction of lack-of-fusion porosity for powder bed fusion," *Additive Manufacturing*, vol. 14, pp. 39–48, 2017.
- [15] T. Mukherjee and T. DebRoy, "Mitigation of lack of fusion defects in powder bed fusion additive manufacturing," *Journal of Manufacturing Processes*, vol. 36, pp. 442–449, 2018.
- [16] M. Bayat, A. Thanki, S. Mohanty, A. Witvrouw, S. Yang, J. Thorborg, N. Tiedje, and J. Hattel, "Keyhole-induced porosities in laser-based powder bed fusion (1-pbf) of ti6al4v: High-fidelity modelling and experimental validation," *Additive Manufacturing*, vol. 30, no. 100835, 2019.
- [17] A. Martin, N. Calta, S. Khairallah, J. Wang, P. Depond, A. Fong, V. Thampy, G. Guss, A. Kiss, K. Stone, C. Tassone, J. Weker, M. Toney, T. van Burren, and M. Matthews, "Dynamics of pore formation during laser powder bed fusion additive manufacturing," *Nature Communications*, vol. 10, no. 1987, 2019.
- [18] A. du Plessis, "Effects of process parameters on porosity in laser powder bed fusion revealed by x-ray tomography," *Additive Manufacturing*, vol. 30, no. 100871, 2019.
- [19] H. Gong, K. Rai, H. Gu, T. Starr, and B. Stucker, "Analysis of defect generation in ti-6al-4v parts made using powder bed fusion additive manufacturing processes," *Additive Manufacturing*, vol. 1-4, pp. 87–98, 2014.
- [20] T. Riipinen, S. Metsä-Kortelainen, T. Lindroos, J. Keränen, A. Manninen, and J. Pippuri-Mäkeläinen, "Properties of soft magnetic fe-co-v alloy produced by laser powder bed fusion," *Rapid Prototyping Journal*, vol. 5, pp. 699–707, 2019.

- [21] L. Criales, Y. Arisoy, B. Lane, S. Moylan, A. Donmez, and T. Özzel, "Laser powder bed fusion of nickel alloy 625: Experimental investigations of effects of process parameters on melt pool size and shape with spatter analysis," *International Journal of Machine Tools and & Manufacture*, vol. 121, pp. 22–36, 2017.
- [22] A. Gaikwad, B. Giera, G. Guss, J. Forien, M. Matthews, and P. Rao, "Heterogeneous sensing and scientific machine learning for quality assurance in laser powder bed fusion a single-track study," *Additive Manufacturing*, vol. 36, no. 101659, 2020.
- [23] L. Meng and J. Zhang, "Process design of laser powder bed fusion of stainless steel using a gaussian process-based machine learning model," *JOM*, vol. 72, no. 1, pp. 420–428, 2020.
- [24] A. Gaikwad, R. Yavari, M. Montazeri, K. Cole, L. Bian, and P. Rao, "Toward the digital twin of additive manufacturing: Integrating thermal simulations, sensing, and analytics to detect process faults," *IISE Transactions*, no. 11, pp. 1204–1217, 2020.
- [25] L. Scime and J. Beuth, "Using machine learning to identify in-situ melt pool signatures indicative of flaw formation in a laser powder bed fusion additive manufacturing process," *Additive Manufacturing*, vol. 25, pp. 151–165, 2019.
- [26] Z. Yang, D. Eddy, S. Krishnamurty, and I. Grosse, "Investigating grey-box modeling for predictive analytics in smart manufacturing," in ASME IDETC/CIE 2017, 2017, pp. DETC2017– 67794.
- [27] J. Francis, A. Sabbaghi, M. Shankar, M. Ghasri-Khouzani, and L. Bian, "Efficient distortion prediction of additively manufactured parts using bayesian model transfer between material systems," *Journal of Manufacturing Science and Engineering*, vol. 142, no. 051001, 2020.
- [28] F. Dugast, P. Apostolou, A. Fernandez, W. Dong, Q. Chen, S. Strayer, R. Wicker, and A. To, "Part-scale thermal process modeling for laser powder bed fusion with matrix-free method and gpu computing," *Additive Manufacturing*, vol. 37, no. 101732, 2021.
- [29] P. Witherell, Y. Zhang, and V. Shapiro, "Towards thermal simulation of powder bed fusion on path level," in *ASME 2019 International Design Engineering Technical Conferences and Computers and Information in Engineering Conference*, Anaheim, CA, USA, August 2019.
- [30] A. Zakirov, S. Belousov, M. Bogdanova, B. Korneev, A. Stepanov, A. Perepelkina, V. Levchenko, A. Meshkov, and B. Potapkin, "Predictive modeling of laser and electron beam powder bed fusion additive manufacturing of metals at the mesoscale," *Additive Manufacturing*, vol. 35, no. 101236, 2020.
- [31] G. Evensen, "The ensemble kalman filter: theoretical formulation and practical implementation," *Ocean Dynamics*, vol. 53, pp. 343–367, 2003.
- [32] N. Wood and D. Hoelzle, "On the controllability and observability of temperature states in powder bed fusion," 2021, submitted to ASME Journal of Dynamic Systems, Measurements, and Control.

- [33] R. Paul, S. Anand, and F. Gerner, "Effect of thermal deformation on part errors in metal powder based additive manufacturing processes," *ASME. J. Manuf. Sci. Eng.*, vol. 136, no. 3, p. 031009, 2014.
- [34] M. Rombouts, L. Froyen, A. V. Gusarov, E. H. Bentefour, and C. Glorieux, "Photopyroelectric measurement of thermal conductivity of metallic powders," *Journal of Applied Physics*, vol. 97, no. 2, p. 024905, 2005.
- [35] R. D. Cook, D. S. Malkus, and M. E. Plesha, *Concepts and Applications of Finite Element Analysis*, 3rd ed. John Wiley and Sons, Inc., 1989.
- [36] S. Greybush, E. Kalnay, T. Miyoshi, K. Ide, and B. Hunt, "Balance and ensemble kalman filter localization techniques," *Monthly Weather Review*, vol. 139, no. 2, pp. 511–522, 2011.
- [37] E. Schwalbach, S. Donegan, M. Chapman, K. Chaput, and M. Groeber, "A discrete source model of powder bed fusion additive manufacturing thermal history," *Additive Manufactur*ing, vol. 25, pp. 485–498, 2019.
- [38] F. Cverna, Ed., *Thermal Properties of Metals*. Materials Park, Ohio: ASM International, 2002.
- [39] M. Patel, "mohakpatel/poisson-disc-sampling (https://github.com/mohakpatel/poisson-disc-sampling), github." retrieved March 19, 2021.